PREDICTING CLUSTER-II-FM6 RE-ENTRY WITH PASSIVE OPTICAL OBSERVATIONS

M. Losacco[1], J. A. Siminski[2], S. Sanvido[1], B. Bastida Virgili[2], S. Lemmens[2], T. Flohrer[2], B. Jilete[3], S. Hawkins[2], F. Ocana[4], M. Micheli[5], O. Kozhukhov[6], L. Shakun[7], P. S. Patole[8], M. Ackermann[8], P. Sauer[8], and T. Schildknecht[8]

[1]*IMS Space Consultancy GmbH at ESA/ESOC Space Debris Office, 64293 Darmstadt, Germany, Email: {matteo.losacco, silvia.sanvido}@ext.esa.int*
[2]*ESA/ESOC Space Debris Office, 64293 Darmstadt, Germany, Email: {jan.siminski, benjamin.bastida.virgili@esa.int, stijn.lemmens@esa.int, tim.flohrer, saskia.hawkins}@esa.int*
[3]*GMV GmbH at ESA/ESAC Space Debris Office, E-28692 Madrid, Spain, Email: beatriz.jilete@ext.esa.int*
[4]*Deimos at ESA/ESAC Planetary Defence Office, E-28692 Madrid, Spain, Email: francisco.ocana@ext.esa.int*
[5]*Starion at ESA/ESRIN Planetary Defence Office, 00044 Frascati, Italy, Email: marco.micheli@ext.esa.int*
[6]*National Space Facilities Control and Test Center of the SSAU, 01010 Kyiv, Ukraine, Email: a.m.kozhukhov@gmail.com*
[7]*Odesa I.I.Mechnikov National University, 65000 Odesa, Ukraine, Email: leomspace@gmail.com*
[8]*Astronomisches Institut - Universität Bern, 3012 Bern, Switzerland, Email: {palash.patole, michael.ackermann2, pascal.sauer, thomas.schildknecht}@unibe.ch*

ABSTRACT

In the evening UTC of 8 September 2024, satellite CLUSTER-II-FM6 eventually closed its 24-year mission, re-entering the Earth's atmosphere over the South Pacific Ocean. The uniqueness of this world-first targeted re-entry was made even more extraordinary by the successful attempt to capture its last stages with an airborne campaign, which produced the first-ever recorded observation of an event of this type. The campaign, organized by ESA's Space Debris Office, required a very accurate prediction of the re-entry location to correctly plan the plane trajectory. Such requirement was made extremely challenging by the concrete possibility of losing the object telemetry during the last orbital revolutions, and by the limited knowledge of the behaviour of the atmosphere during the last perigee pass, having a potentially tremendous impact on the actual re-entry epoch and location.

To guarantee the availability of data till the last phases of the re-entry and at the same time investigate the feasibility and accuracy of a purely passive optical-based re-entry prediction, an observation campaign involving passive optical telescopes was carried out since May 2024. Several actors contributed to the observation of Salsa, including ESA's Planetary Defence Office, the State Space Agency of Ukraine, and the Astronomical Institute of the University of Bern.

This paper illustrates the results of the optical observation campaign. The first part of the paper describes the trend of the re-entry estimate during the last weeks of observations, showing a comparison with telemetry-based predictions and their sensitivity against uncertainties in the drag coefficient. The second part illustrates the orbit determination strategy adopted for the last revolution. Given the expected strong impact of the atmosphere during the last perigee pass, a strategy based on the processing of observations acquired only after this pass was selected. The a-priori analyses performed to support this decision are shown, illustrating the feasibility of an orbit determination solution, its robustness against the expected inaccuracy in the initial guess, the sensitivity of the estimate on the number of observing stations and coverage of the orbital arc, and the impact of the atmosphere during the last portion of the re-entry arc. Finally, the paper illustrates the results obtained by processing the real data acquired during the two nights between the last perigee pass and the re-entry epoch, showing the variability of the solution with number of sensors and data involved, its agreement with telemetry-based predictions, and a post-processing of the results, illustrating how the inclusion of pre-perigee pass data could have affected the accuracy and uncertainty of the obtained re-entry estimate.

Keywords: Orbit determination; passive optical telescopes; re-entry predictions; CLUSTER-II-FM6.

1. BACKGROUND

When searching for the term "replicability" in science, the following definition can be found: "The possibility of obtaining consistent results across studies aimed at answering the same scientific question using new data or

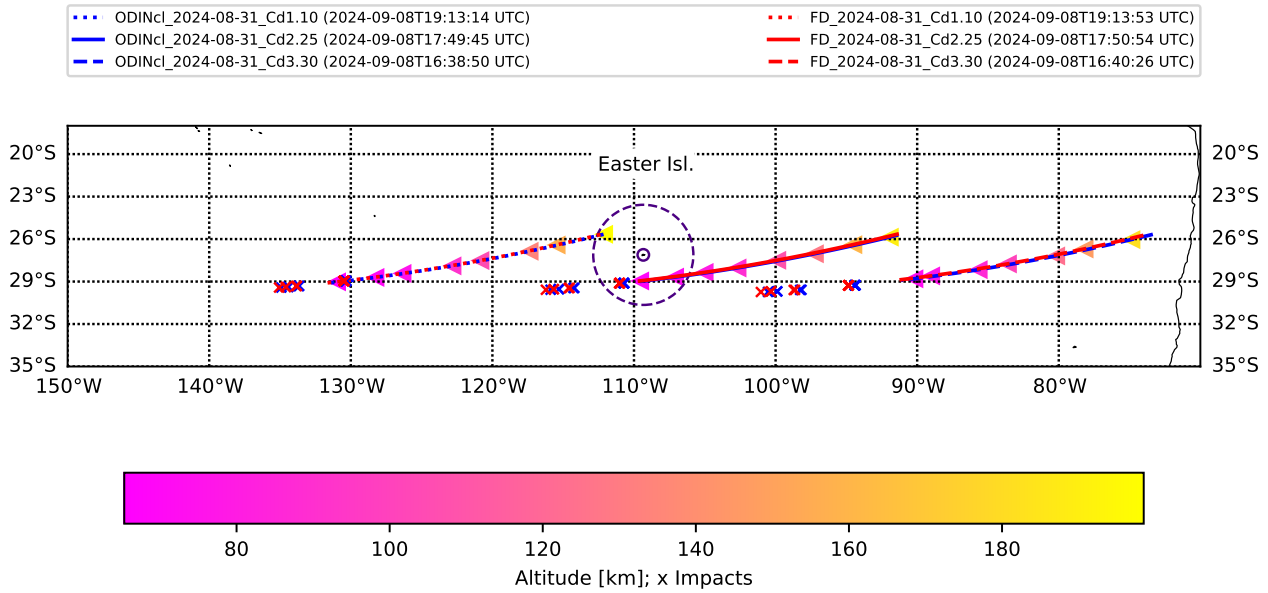

Figure 1: Re-entry ground track as a function of $c_{d,prop}$ and OD method. In red, telemetry-based results; in blue, optical-based estimates. Crosses represent impact location of estimated fragments. The results are obtained based on the FD ephemeris issued on 31 August 2024.

$c_{d,prop}$	P-3	P-2	P-1
1.10	54.13	54.08	52.81
2.25	54.11	54.01	51.51
3.30	54.09	53.95	50.42

Table 1: CLUSTER-II-FM6 estimated orbital period after each perigee pass. Values are obtained by extracting FD OD state on 31 August 2024 and propagating it with different values of drag coefficient $c_{d,prop}$. All values are in hours.

other new computational methods"[1]. Setting up a repeatable experiment is of great importance for validating new models or correcting existing ones. However, this requires on one side some constant conditions that are maintained from experiment to experiment and on the other side an accurate estimation of the possible sources of uncertainty that the variation of the other parameters and external conditions might introduce. A mismodelling of such uncertainties might undermine any conclusion and the replicability of the experiment itself.

Now imagine this scenario: four spacecraft, all with the same mass, area, shape; all placed on similar orbits whose long-term dynamics is driven by the luni-solar gravitational perturbation, making their evolution predictable years in advance; all supposed to re-enter in short sequence one after the other, with the possibility of targeting a specific re-entry spot on Earth. If one had to choose a framework for setting up a repeatable experiment on the effect of the atmosphere on re-entering objects, wouldn't this be the ideal one?

[1] https://www.nationalacademies.org/news/2019/09/reproducibility-and-replicability-in-research

These were probably the considerations that were made when the Space Debris Office (SDO) of the European Space Agency (ESA) had the idea of trying to capture the latest phases of the re-entry of satellite CLUSTER-II-FM6 while observing it with an airborne campaign. The concept was easy: if the re-entry region can be determined well in advance with enough accuracy, one can try to fly a plane where the fragmentation is supposed to happen, and observe the event with cameras and spectrographs. Starting from these considerations, a consortium including Hypersonic Technology Göttingen (HTG), Astros Solution, University of Stuttgart (IRS/HEFDiG), Comenius University in Bratislava (CUB), and the University of Southern Queensland (UniSQ) was organized by ESA with the goal of studying the feasibility of observing the breakup of the satellite flying a plane from Easter Island. Two were the necessary (but not sufficient) conditions for a successful attempt: an extremely accurate prediction of the re-entry location, and a stability of such prediction in the last day of the re-entry campaign. The task for ESA, and specifically for SDO, was to study whether these requirements could be met.

Unfortunately, it was evident since the very beginning that, though the luni-solar perturbation was the main driver for the long-term orbital evolution, the final stages of the re-entry phase would deal with an actor whose behaviour is much less predictable: the atmosphere. Table 1 shows the variability of CLUSTER-II-FM6 orbital period along the last revolution arcs as a function of the drag coefficient used for the propagation. The results were obtained by considering the orbital state estimated by ESA Flight Dynamics (FD) team on 31 August 2024, and then propagating this state with a high-fidelity numerical propagator with drag coefficient $c_{d,prop}$ equal to 1.10, 2.25, and 3.30. The 2.25 represented our baseline scenario,

OD epoch	$c_{d,prop}$	Telemetry-based	Optical-based
2024-08-31	1.10	2024-09-08T19:13:53	2024-09-08T19:13:14
	2.25	2024-09-08T17:50:54	2024-09-08T17:49:45
	3.30	2024-09-08T16:40:26	2024-09-08T16:38:50
2024-09-03	1.10	2024-09-08T19:11:29	2024-09-08T19:11:07
	2.25	2024-09-08T17:50:26	2024-09-08T17:49:36
	3.30	2024-09-08T16:40:46	2024-09-08T16:39:38
2024-09-04	1.10	2024-09-08T19:07:27	2024-09-08T19:07:37
	2.25	2024-09-08T17:50:46	2024-09-08T17:50:38
	3.30	2024-09-08T16:43:27	2024-09-08T16:42:59
2024-09-05	1.10	2024-09-08T19:07:19	2024-09-08T19:06:59
	2.25	2024-09-08T17:50:30	2024-09-08T17:49:59
	3.30	2024-09-08T16:43:01	2024-09-08T16:42:13

Table 2: Historical trend of telemetry-based and optical-based re-entry predictions as a function of the drag coefficient $c_{d,prop}$.

while the two extremes were chosen assuming an uncertainty in the atmospheric model up to 50% [1]. As can be seen, the delta between the two extremes progressively increases, passing from 2 min after P-3 to around 8 min after the second last perigee pass. But such variations are almost negligible if compared to those induced by the last perigee pass (P-1), occurring at around 14 UTC of 6 September 2024. Here, the predicted orbital period passes from around 52 h 49 min of the $c_{d,prop}$ = 1.10 case to 50 h and 25 min with $c_{d,prop}$ = 3.30. That is, according to the considered drag coefficient, the resulting orbital periods would differ up to almost 2.5 h.

In order to better visualize what such a difference would mean, Fig. 1 shows the estimated ground-tracks for the three cases investigated. The telemetry-based $c_{d,prop}$ = 3.30 case is represented with a red dashed line (extreme right), whereas the $c_{d,prop}$ = 1.10 estimate is reported with a dotted line (extreme left). As can be seen, the orbital period difference turns into a delta in longitude of about 35 deg, while no deviation in latitude is expected. It is apparent that such an uncertainty would shatter any hope to successfully observe the re-entry from the plane.

In addition to the uncertainty introduced by the atmosphere, the possibility of losing the object telemetry and thus FD predictions during the last perigee pass was a scenario which could not be ruled out. Such an eventuality, if occurred, without any other independent sources of information for predicting the orbital state of the object, would have eventually brought the curtain down on the airborne campaign experiment. Given the necessity of having a backup solution in case of loss of telemetry data, and in order to investigate the feasibility and accuracy of a purely passive optical observations-based re-entry prediction, an observation campaign involving several sensors was started in May 2024. Three main institutions took part to the experiment with their sensors, namely ESA's Planetary Defence Office (PDO) with OGS, CAHA and K91 sensors [2], the State Space Agency of Ukraine (SSAU) with sensors OES30, OES35, and OES50 [3], and the Astronomisches Institut - Universität Bern (AIUB) with ZIMLAT, ZimMAIN and ZimTWIN sensors [4]. The first months of the campaign were used to assess the feasibility of observing such a peculiar target, while the last two weeks before re-entry a first comparison between telemetry-based and optical-based predictions was carried out. Table 2 shows this comparison for the final days before the last perigee pass, parametrised with respect to the drag coefficient, while a comparison in predicted ground-tracks is shown in Fig. 1 (blue lines).

All optical-based orbit determination (OD) predictions of this first phase considered an observation arc of 1 or 2 weeks in the past. As the last perigee pass epoch approached, two questions became more and more pressing: will we be still able to obtain an accurate re-entry prediction after this pass also in case of loss of telemetry? And if so, how stable will our solution be? Without an answer, a GO to the airborne campaign could not be given. Therefore, a proper analysis was required.

2. OD STRATEGY JUSTIFICATION

The expected strong variability of the re-entry epoch induced by the last perigee pass represented the driver for the selection of the OD strategy. Two alternative approaches were available. The first consisted in processing observations acquired both before and after P-1. This approach had the advantage of offering a longer arc to process. At the same time, it required a propagation through the P-1 pass during the fitting, which, considering the possible inaccuracies in the modelled behaviour of the atmospheric drag, could had led to either convergence problems or inaccurate solutions. The second option was to consider observations acquired only after P-1. This solution was considered immediately appealing as it had a clear advantage: if the fitting is performed by processing observations acquired after P-1, the impact of the atmosphere becomes null, so any convergence problem related to the mismodelling of the drag perturbation would disappear. On the other hand, the possible limitations and risks of such an approach had to be analysed, namely the sensitivity of the OD convergence to errors in initial guess, the variability of the solution with the number of available data, and its stability across the whole two-night observation campaign.

	Night_1	$\text{Night}_{1,2}$
OGS	125.40 km	279.06 km
OGS + CAHA	289.30 km	314.92 km
OGS + CAHA + OES35	314.92 km	331.81 km

Table 3: OD convergence radius in terms of maximum position error in OD initial guess as a function of number of involved sensors and observation arc.

The simulations performed to investigate the feasibility and robustness of an OD solution based on the processing of only post P-1 data are presented hereafter. All the analyses were done by considering some basic assumptions about the reference orbit, the number of sensors involved, and the frequency of observations. The reference orbit used to generate synthetic optical observations was derived from the OD product provided by FD on 4 September 2024. More specifically, the OD state $\boldsymbol{x}_{FD}$ was propagated from its reference epoch till re-entry with a high-fidelity numerical propagator assuming a value for the drag coefficient equal to 2.25, which was considered as baseline for our analyses. Then, noisy measurements were generated over three different sensors, i.e. OGS, CAHA and OES35. This set of sensors was selected as considered the minimum set available during the two-night observation campaign. Different observation windows and frequencies for the three sensors were chosen, i.e.

- OGS: 1 tracklet of 10 min per hour, with 1 observation per minute, from 2024-09-06T20:00 UTC to 2024-09-07T03:10 UTC (Night_1) plus 3 tracklets of 10 min each, with 1 observation per minute, starting at 2024-09-07T20:00 UTC, 2024-09-07T23:00 UTC, and 2024-09-08T03:00 UTC respectively (Night_2);
- CAHA: 1 tracklet of 10 min per hour, with 1 observation per minute, from 2024-09-06T20:00 UTC to 2024-09-07T03:10 UTC (Night_1);
- OES35: 2 tracklets of 10 min, with 1 observation per minute, starting at 2024-09-06T22:00 UTC and 2024-09-07T22:00 UTC, respectively.

Once generated the set of possible available measurements, a first analysis aiming at investigating the impact of errors in the initial guess on the convergence of the OD process was done. A pool of possible initial guesses was generated by exploiting the sensitivity of the orbital propagation result to the atmospheric drag during P-1. More specifically, the reference state $\boldsymbol{x}_{FD}$ was propagated till re-entry considering a fan of possible c_d values ranging from 1.1 to 3.3. This set of ephemerides was then used as possible initial guesses during the OD process, and the dependency of the convergence of the OD solution on the error in the initial input analysed. The results are shown in Table 3. The table shows the convergence radius of the OD process as a function of number of sensors involved and duration of the observation window. The considered orbit determination tool used for the analyses is the ODIN software [5]. All main perturbations were considered, namely the zonal/tesseral effects of the Earth's gravitational field up to order and degree 36, the gravitational pull of Sun and Moon, the solar radiation pressure, and the drag perturbation. Three different sensor configurations were selected, namely OGS alone, OGS and CAHA, and a third scenario including OES35. As for the observation window, the datasets available at the end of the first (Night_1) and second ($\text{Night}_{1,2}$) night were considered. The estimation process was performed by selecting the same OD epoch (2024-09-07T00:00:39.879 UTC) for all scenarios. As a result, errors in the initial guess up to 585 km were obtained. Two expected trends can be identified. The maximum allowed error increases as number of observing sensors and observed arc length increase. Overall, by passing from the one-night, OGS-only scenario to the two-night, all sensors case, the convergence radius inflates, passing from 125.40 km to 331.81 km. Though apparently significant, such error levels can be easily achieved with minor mismodelling of the atmospheric drag. As an example, the 125.40 km error initial guess was obtained by propagating $\boldsymbol{x}_{FD}$ with c_d equal to 2.02, while the 331.81 km case was obtained by considering c_d equal to 2.9. As a result, it was immediately evident that, had a post P-1 only strategy been followed, care in the selection of the initial guess should have been taken. Multiple alternatives were studied and prepared, ranging from initial orbit determination algorithms to the aforementioned generation of fans of possible initial guesses based on multiple propagations of the latest orbital information over different c_d. In the end, it was clear that this aspect would be a critical point of the estimation process.

Once assessed the feasibility of an OD solution, the second aspect investigated was the sensitivity of the OD-derived re-entry estimate on number of sensors and observed arc length and its consistency throughout the two-night observation campaign. The results are shown in Table 4. The table shows, for different observation conditions, the estimated re-entry epoch, as obtained by propagating the obtained OD solution till re-entry, here defined at 70 km altitude. In addition, the variability of this estimate when different c_d are used to propagate the OD solution is investigated. Let us first analyse the ideal case, so let us consider entries with c_d equal to 2.25, let us focus on the OGS-only case, and see how the re-entry prediction changes while passing from one to two nights of observation. As can be seen, the one-night estimate (2024-09-08T17:48:05.790 UTC) is about 3 minutes earlier than the two-night prediction (2024-09-08T17:51:12.245 UTC). As the number of involved sensors increases, the two-night prediction remains almost unaltered, whereas the delta with the single-night estimate significantly shrinks. More specifically, for the OGS-CAHA case, the difference between the one-night prediction (2024-09-08T17:50:35.733 UTC) and the two-night estimate (2024-09-08T17:51:11.444 UTC) is less than 40 s, while if OES35 is added, the difference is about 15 s. This result was used as a criterion for the selection of the minimum number of participants needed. A re-

	$c_{d,prop}$	Night_1	$\text{Night}_{1,2}$
OGS	1.10	2024-09-08T17:48:05.435	2024-09-08T17:51:13.592
	2.25	2024-09-08T17:48:05.790	2024-09-08T17:51:12.245
	3.30	2024-09-08T17:48:06.113	2024-09-08T17:51:11.564
OGS, CAHA	1.10	2024-09-08T17:50:35.793	2024-09-08T17:51:12.726
	2.25	2024-09-08T17:50:35.733	2024-09-08T17:51:11.444
	3.30	2024-09-08T17:50:35.751	2024-09-08T17:51:10.792
OGS, CAHA, OES35	1.10	2024-09-08T17:50:56.449	2024-09-08T17:51:12.069
	2.25	2024-09-08T17:50:56.106	2024-09-08T17:51:10.839
	3.30	2024-09-08T17:50:55.944	2024-09-08T17:51:10.211

Table 4: Re-entry prediction stability and dependency on drag coefficient as a function of number of involved sensors and observation arc. Reference re-entry epoch is 2024-09-08T17:51:11.332 UTC.

quirement from the plane mission was indeed to have a variability of the OD solution from the end of Night_1 to the end of Night_2 of 20 s at maximum. As the analyses show, this was potentially achievable only by involving three or more non-co-located sensors since Night_1.

It is now interesting to study the impact on the re-entry prediction of the selection of the drag coefficient used to propagate the OD estimate. As anticipated at the beginning of this section, the benefit of performing OD over post P-1 only observations is to completely eliminate the drag perturbation from the orbit estimation process. This is certainly valid for the fitting process, but does not hold for the re-entry prediction phase, as the required propagation includes in the very last part of the re-entry arc a portion in the atmosphere. Since the c_d is essentially unknown at this stage, as it cannot be estimated anymore, we need to check what is the effect of using different c_d on the re-entry prediction. The analysis is shown in Table 4. As can be seen, regardless of the scenario considered, the maximum variability that can be observed within the same scenario due to different drag coefficients is always less than 2 s. Therefore, we can conclude that an effect of the selection of c_d in the estimation of the re-entry prediction exists, but is marginal. Overall, if we compare the prediction obtained by processing all the observations from the three sensors over the two nights and considering the extreme values for c_d, the errors obtained with respect to the simulated ground truth (2024-09-08T17:51:11.332 UTC) are in the order of 1-2 s.

In summary, the main conclusion of the analysis was clear: a reliable and stable re-entry prediction purely based on post P-1 only optical observations was perfectly achievable, provided that multiple sensors participated in the campaign and the initial OD guess was properly selected. This conclusion was used as justification for the selection of the described OD strategy as baseline for the final two-night observation campaign.

3. RESULTS

This section illustrates the results of the two-night observation campaign. Two crucial elements had a positive effect on the estimation process, namely the number of participating sensors, which was significantly beyond expectations, and the spacecraft behaviour during the last perigee pass. Overall, 8 sensors contributed to the campaign during the two nights, namely ESA PDO's OGS, CAHA and K91, AIUB's ZIMLAT (ZIML), ZimMAIN (ZIMN) and ZimTWIN (ZIMT), and SSAU's OES35 and OES50. This aspect significantly favoured the stability of the solution, as later described. In addition, the functional integrity of the satellite was preserved during P-1, and telemetry data could be acquired and processed by FD throughout the last revolution arc. Three updated orbital ephemerides were delivered by FD during the two-night campaign, namely on 2024-09-06T20:00 UTC, 2024-09-07T00:00 UTC and 2024-09-07T17:30 UTC, and they were used as initial guess for the optical-based estimation process. A fourth prediction was later provided post-event. Such prediction will be used here as term of comparison for assessing the quality of our results.

Figure 2 shows the result of the orbit determination process in terms of residuals in topocentric right ascension α and declination δ as obtained by processing all the observations collected by all the sensors during the two nights. The "+" symbol is used for accepted measurements, while rejected data points are marked with a "x", for an overall number of observations equal to 1584. The observed arc covers the time window from 2024-09-06T19:18:16 UTC to 2024-09-08T02:03:03 UTC, i.e about 35 deg of true anomaly variation across the apogee pass, from 153.5 deg to 187.9 deg. The OD epoch is placed at the middle point of the observation arc (2024-09-07T11:04:08 UTC), while the initial guess is extracted by the available FD orbital information. The OD process results into a 100% acceptance of all processed data, with the root mean square error in α and δ equal to 0.266 arcsec and 0.176 arcsec, respectively. The osculating mean value and standard deviation of the Keplerian parameters, namely semi-major axis a, eccentricity e, inclination i, right ascension of the ascending node (RAAN) Ω, argument of perigee (AoP) ω and true anomaly ϑ, are [71 124.0 km, 0.909, 150.32 deg, 39.92 deg, 256.60 deg, 175.6 deg] and [0.6 km, 1.5e−6, 4.0e−5, 1.4e−4 deg, 2.6e−4 deg, 3.0e−4 deg], respectively. The estimated state was then propagated with a high fidelity numerical propagator till re-entry epoch (70 km altitude). The c_d used for the propagation was the one estimated by FD during their first OD batch, 1.72. As a result, the esti-

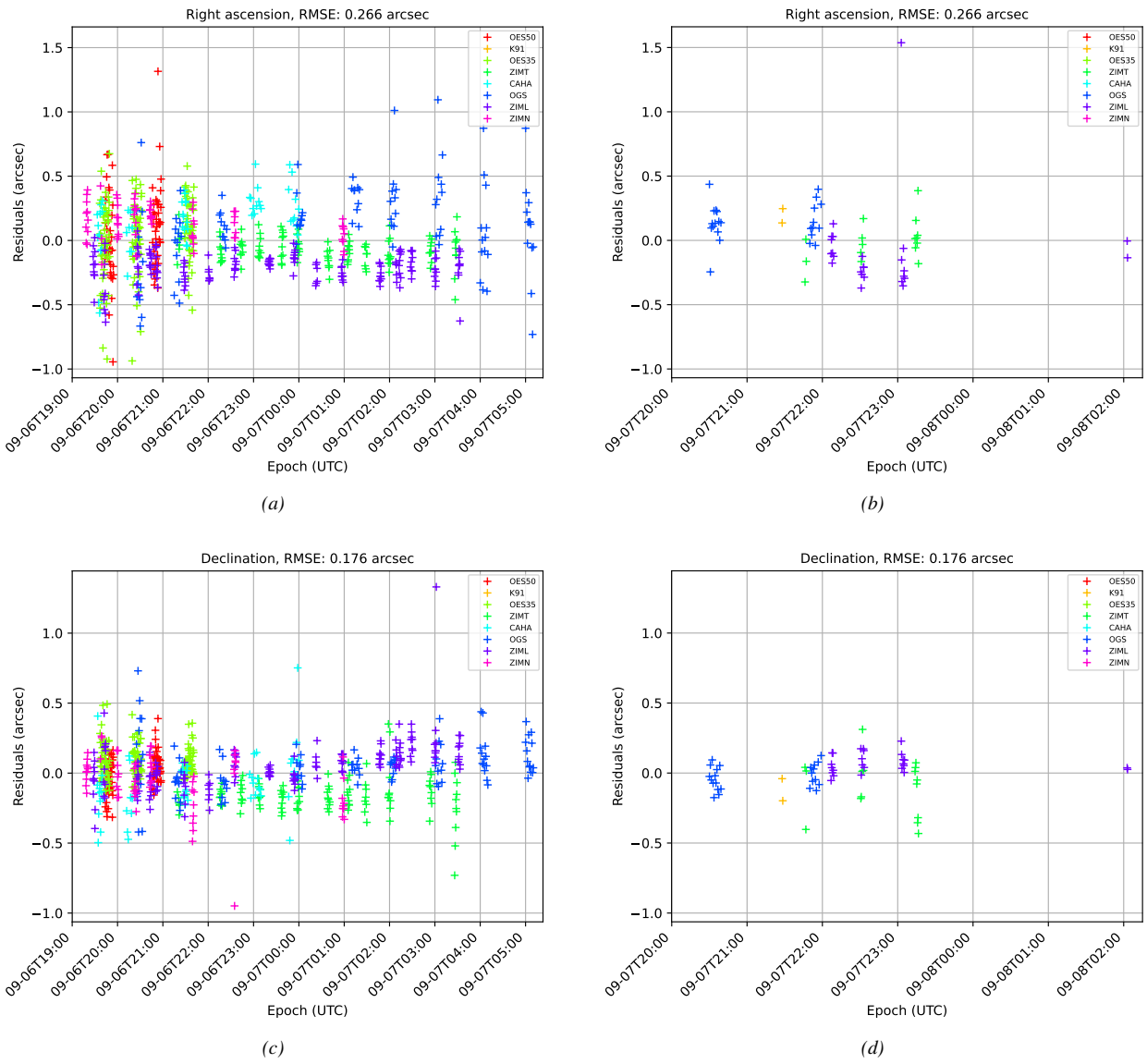

Figure 2: Orbit determination result in terms of residuals in topocentric right ascension and declination as obtained by processing all observations collected by all sensor throughout the two-night campaign; (a) topocentric right ascension, Night$_1$ data; (b) topocentric right ascension, Night$_2$ data; (c) topocentric declination, Night$_1$ data; (d) topocentric declination, Night$_2$ data.

#	Epoch$_0$	Epoch$_f$
1	2024-09-06T19:00:00	2024-09-07T00:00:00
2	2024-09-06T19:00:00	2024-09-07T02:00:00
3	2024-09-06T19:00:00	2024-09-07T04:00:00
4	2024-09-06T19:00:00	2024-09-07T06:00:00
5	2024-09-06T19:00:00	2024-09-08T00:00:00
6	2024-09-06T19:00:00	2024-09-08T04:00:00

Table 5: Observation batches definition, in terms of initial epoch Epoch$_0$ and final epoch Epoch$_f$. All epochs are UTC.

	Participants
O	OES35
PDO$_1$	OGS
PDO$_2$	OGS, CAHA, K91
AIUB$_1$	ZIML
AIUB$_2$	ZIML, ZIMN, ZIMT
ALL	OES35, OES50, OGS, CAHA, K91, ZIML, ZIMN, ZIMT

Table 6: Networks participants.

mated re-entry date was 2024-09-08T18:47:36.6 UTC.

An analysis of the sensitivity of the re-entry prediction on number of sensors and observed arc length was performed. Different batches of observations progressively covering both nights and different combinations of sensors were defined, and the variability of the OD result and re-entry prediction studied. This analysis was done to

	#	$\text{Epoch}_{\text{TDM},0}$	$\text{Epoch}_{\text{TDM},f}$	ϑ_0 (deg)	ϑ_f (deg)	Epoch_{OD}	Epoch_{RE}
O	1	2024-09-06T19:36:28.3	2024-09-06T21:40:57.6	154.5	159.7	2024-09-06T20:45:24.3	2024-09-08T18:48:07.4
PDO_1	1	2024-09-06T20:25:06.6	2024-09-06T23:58:39.8	156.8	163.7	2024-09-06T22:13:15.9	2024-09-08T18:51:19.3
	2	2024-09-06T20:25:06.6	2024-09-07T01:20:05.3	156.8	165.7	2024-09-06T23:03:08.3	2024-09-08T18:49:06.4
	3	2024-09-06T20:25:06.6	2024-09-07T03:10:00.6	156.8	168.0	2024-09-06T23:57:09.1	2024-09-08T18:48:08.4
	4	2024-09-06T20:25:06.6	2024-09-07T05:10:14.7	156.8	170.2	2024-09-07T00:55:23.4	2024-09-08T18:47:40.5
	5	2024-09-06T20:25:06.6	2024-09-07T21:58:58.3	156.8	184.3	2024-09-07T09:36:18.3	2024-09-08T18:47:44.8
PDO_2	1	2024-09-06T19:33:12.9	2024-09-06T23:59:57.9	154.3	163.8	2024-09-06T21:57:32.4	2024-09-08T18:48:04.3
	2	2024-09-06T19:33:12.9	2024-09-07T01:20:05.3	154.3	165.7	2024-09-06T22:29:26.2	2024-09-08T18:48:08.4
	3	2024-09-06T19:33:12.9	2024-09-07T03:10:00.6	154.3	168.0	2024-09-06T23:38:40.8	2024-09-08T18:47:53.7
	4	2024-09-06T19:33:12.9	2024-09-07T05:10:14.7	154.3	170.2	2024-09-07T00:35:30.2	2024-09-08T18:47:35.7
	5	2024-09-06T19:33:12.9	2024-09-07T21:58:58.3	154.3	184.3	2024-09-07T09:07:35.5	2024-09-08T18:47:41.6
AIUB_1	1	2024-09-06T19:27:44.5	2024-09-06T23:55:02.8	154.1	163.7	2024-09-06T21:42:15.4	2024-09-08T18:48:20.3
	2	2024-09-06T19:27:44.5	2024-09-07T01:48:56.6	154.1	166.3	2024-09-06T22:46:03.5	2024-09-08T18:47:59.2
	3	2024-09-06T19:27:44.5	2024-09-07T03:33:35.3	154.1	168.4	2024-09-06T23:38:40.8	2024-09-08T18:48:06.4
	5	2024-09-06T19:27:44.5	2024-09-07T23:05:25.7	154.1	185.2	2024-09-07T09:36:18.3	2024-09-08T18:47:39.7
	6	2024-09-06T19:27:44.5	2024-09-08T02:03:03.4	154.1	187.9	2024-09-07T11:04:08.7	2024-09-08T18:47:37.7
AIUB_2	1	2024-09-06T19:18:16.2	2024-09-06T23:59:53.6	153.5	163.8	2024-09-06T21:42:15.4	2024-09-08T18:48:07.6
	2	2024-09-06T19:18:16.2	2024-09-07T01:59:31.6	153.5	166.6	2024-09-06T22:46:03.5	2024-09-08T18:48:01.6
	3	2024-09-06T19:18:16.2	2024-09-07T03:33:35.3	153.5	168.4	2024-09-06T23:38:40.8	2024-09-08T18:48:08.4
	5	2024-09-06T19:18:16.2	2024-09-07T23:16:30.8	153.5	185.4	2024-09-07T09:36:18.3	2024-09-08T18:47:41.8
	6	2024-09-06T19:18:16.2	2024-09-08T02:03:03.4	153.5	187.9	2024-09-07T11:04:08.7	2024-09-08T18:47:39.6
ALL	1	2024-09-06T19:18:16.2	2024-09-06T23:59:57.9	153.5	163.8	2024-09-06T21:42:15.4	2024-09-08T18:47:38.6
	2	2024-09-06T19:18:16.2	2024-09-07T01:59:31.6	153.5	166.6	2024-09-06T22:46:03.5	2024-09-08T18:47:29.6
	3	2024-09-06T19:18:16.2	2024-09-07T03:33:35.3	153.5	168.4	2024-09-06T23:38:40.8	2024-09-08T18:47:32.6
	4	2024-09-06T19:18:16.2	2024-09-07T05:10:14.7	153.5	170.2	2024-09-07T00:16:05.5	2024-09-08T18:47:36.0
	5	2024-09-06T19:18:16.2	2024-09-07T23:16:30.8	153.5	185.4	2024-09-07T09:36:18.3	2024-09-08T18:47:36.7
	6	2024-09-06T19:18:16.2	2024-09-08T02:03:03.4	153.5	187.9	2024-09-07T11:04:08.7	2024-09-08T18:47:36.6
FD							2024-09-08T18:47:37.2

Table 7: Re-entry prediction parameters and estimate as a function of network of sensors and observation batch (#), i.e. OD arc initial and final epochs $\text{Epoch}_{\text{TDM},0}$ and $\text{Epoch}_{\text{TDM},f}$, initial and final true anomalies ϑ_0 and ϑ_f, OD epoch Epoch_{OD} and estimated re-entry epoch Epoch_{RE}. All epochs are UTC.

check whether the figures obtained during the OD strategy selection phase were confirmed. Table 5 shows the selected observation batches. Six different batches were selected. The first four batches progressively cover the first night, starting from a 5-hour coverage of batch 1 to the full night coverage of batch 4, which lasts from 2024-09-06T19:00 UTC to 2024-09-07T06:00 UTC. The last two batches include the first observations slots of the second night with batch 5 and finally cover both nights with batch 6. Table 6 instead lists the telescope networks considered in this analysis. Six different networks were selected, namely O, PDO_1, PDO_2, AIUB_1, AIUB_2 and ALL. Details about the network composition are provided in the table. Two main groups can be identified, namely single-sensor networks (O, PDO_1 and AIUB_1) and multiple-sensor networks (PDO_2, AIUB_2 and ALL). The former are included in order to study the feasibility of a re-entry prediction by relying on just one sensor. .

The results of the sensitivity analysis are shown in Tables 7 and 8. Table 7 shows the re-entry prediction inputs and result as a function of network of participants and observation batch. Specifically, the table shows the start and end epochs of the OD arc $\text{Epoch}_{\text{TDM},0}$ and $\text{Epoch}_{\text{TDM},f}$, the initial and final true anomalies ϑ_0 and ϑ_f, the OD epoch Epoch_{OD} and the estimated re-entry epoch at 70 km altitude Epoch_{RE}. The last line reports the re-entry prediction as obtained by propagating the FD post-event estimate, i.e. our reference. As expected, the accuracy of the re-entry estimate improves as the arc coverage increases. The trend is generally not monotonic, as can be seen e.g. by looking at the re-entry prediction for AIUB_1. Overall, if we study the variability of the estimate within a specific multiple-sensor network we can see that such variation is very limited, ranging from about 33 s of PDO_2 to 9 s when all sensors are included. The performance of single-sensor networks is somehow more limited. A clear example is shown by the PDO_1 case, where only OGS is used. Here the variation between batches 1 and 5 is around 3.5 min. It is worth noticing, however, that this case is also the one with the latest first observation (2024-09-06T20:25:06.6 UTC), thus the arc coverage of the initial batches is smaller than for the other ones, which could explain the lower accuracy achieved by the sensor alone during the early observation batches. If we look at the results obtained from batch 3 on, we can see that the offset with respect to the reference shrinks, passing from about 30 s (batch 3) to 7 s (batch 6). Better results can be obtained if the overall arc coverage is larger. If we look at the AIUB_1 case, we can see that the offset of the solution with respect to the reference is of just 43 s in batch 1, and at the end of the two-night campaign is only of 0.5 s. This result is quite impressive, as it shows that a single-sensor network can achieve an extremely good re-entry predic-

	#	$[\varepsilon_a; \sigma_a]$ (km)	$[\varepsilon_e; \sigma_e]$ (-)	$[\varepsilon_i; \sigma_i]$ (deg)	$[\varepsilon_\Omega; \sigma_\Omega]$ (deg)	$[\varepsilon_\omega; \sigma_\omega]$ (deg)	$[\varepsilon_\vartheta; \sigma_\vartheta]$ (deg)
O	1	[7.2; 158.4]	[4.9e−6; 7.1e−5]	[1.9e−4; 5.5e−4]	[1.1e−4; 3.2e−3]	[1.3e−3; 4.8e−2]	[5.4e−3; 1.0e−1]
PDO_1	1	[30.1; 101.2]	[4.2e−5; 1.2e−4]	[4.3e−4; 9.8e−4]	[8.4e−4; 3.0e−3]	[9.8e−3; 3.4e−2]	[1.8e−2; 6.1e−2]
	2	[17.9; 47.9]	[2.4e−5; 6.2e−5]	[2.8e−4; 3.7e−4]	[3.6e−4; 1.2e−3]	[5.8e−3; 1.7e−2]	[1.0e−2; 2.8e−2]
	3	[6.6; 24.0]	[1.1e−5; 3.4e−5]	[2.5e−4; 3.4e−4]	[2.6e−4; 1.1e−3]	[1.8e−3; 9.3e−3]	[3.7e−3; 1.4e−2]
	4	[0.5; 13.8]	[5.4e−6; 2.0e−5]	[2.8e−4; 3.2e−4]	[3.8e−4; 1.0e−3]	[3.3e−4; 5.8e−3]	[8.3e−5; 8.0e−3]
	5	[1.6; 2.8]	[3.8e−6; 6.0e−6]	[2.0e−4; 7.9e−5]	[8.2e−5; 3.2e−4]	[2.3e−4; 1.1e−3]	[8.0e−4; 1.4e−3]
PDO_2	1	[6.1; 12.1]	[1.5e−6; 1.5e−5]	[4.0e−4; 3.3e−4]	[7.7e−4; 1.0e−3]	[8.7e−4; 3.9e−3]	[4.2e−3; 7.8e−3]
	2	[6.9; 11.6]	[4.1e−6; 1.3e−5]	[4.0e−4; 2.6e−4]	[8.0e−4; 8.4e−4]	[1.2e−3; 3.8e−3]	[4.5e−3; 7.4e−3]
	3	[3.6; 9.6]	[3.0e−6; 1.1e−5]	[3.6e−4; 1.9e−4]	[6.7e−4; 6.1e−4]	[3.3e−4; 3.4e−3]	[2.3e−3; 5.9e−3]
	4	[0.4; 7.2]	[1.3e−6; 9.4e−6]	[3.5e−4; 1.6e−4]	[6.2e−4; 5.0e−4]	[9.2e−4; 2.7e−3]	[3.7e−4; 4.3e−3]
	5	[0.9; 1.9]	[2.2e−6; 4.0e−6]	[2.3e−4; 7.0e−5]	[2.2e−4; 2.7e−4]	[1.3e−4; 7.3e−4]	[4.8e−4; 9.8e−4]
$AIUB_1$	1	[9.5; 43.1]	[5.9e−6; 3.1e−5]	[2.2e−4; 3.3e−4]	[4.9e−4; 1.3e−3]	[2.5e−3; 1.4e−2]	[6.2e−3; 2.8e−2]
	2	[4.7; 21.3]	[5.6e−6; 1.8e−5]	[2.6e−4; 2.7e−4]	[5.4e−4; 7.0e−4]	[1.1e−3; 7.2e−3]	[2.9e−3; 1.3e−2]
	3	[6.3; 13.1]	[6.7e−6; 1.2e−5]	[2.6e−4; 2.4e−4]	[5.8e−4; 5.5e−4]	[1.5e−3; 4.7e−3]	[3.9e−3; 8.2e−3]
	5	[0.5; 2.0]	[1.1e−6; 5.1e−6]	[2.4e−4; 7.7e−5]	[3.2e−4; 2.6e−4]	[2.5e−4; 8.5e−4]	[3.2e−4; 9.6e−4]
	6	[0.1; 1.2]	[6.1e−8; 3.4e−6]	[2.4e−4; 7.1e−5]	[3.1e−4; 2.5e−4]	[4.1e−4; 5.6e−4]	[1.2e−4; 5.9e−4]
$AIUB_2$	1	[6.7; 28.3]	[4.3e−6; 2.0e−5]	[5.2e−5; 2.2e−4]	[7.7e−5; 8.9e−4]	[2.1e−3; 8.9e−3]	[4.4e−3; 1.8e−2]
	2	[5.2; 13.8]	[5.3e−6; 1.2e−5]	[8.3e−5; 1.8e−4]	[1.6e−6; 4.7e−4]	[1.7e−3; 4.7e−3]	[3.3e−3; 8.7e−3]
	3	[6.7; 8.8]	[7.2e−6; 8.4e−6]	[1.0e−4; 1.6e−4]	[9.4e−5; 3.9e−4]	[2.1e−3; 3.2e−3]	[4.2e−3; 5.5e−3]
	5	[0.9; 1.3]	[2.3e−6; 3.4e−6]	[1.8e−4; 5.7e−5]	[1.8e−4; 1.9e−4]	[3.7e−5; 5.8e−4]	[5.2e−4; 6.5e−4]
	6	[0.4; 1.0]	[1.2e−6; 2.7e−6]	[1.9e−4; 5.5e−5]	[1.8e−4; 1.9e−4]	[1.5e−4; 4.6e−4]	[3.0e−4; 4.9e−4]
ALL	1	[0.3; 4.5]	[6.7e−8; 4.1e−6]	[1.3e−4; 1.5e−4]	[5.9e−5; 4.6e−4]	[1.1e−4; 1.3e−3]	[2.4e−4; 3.2e−3]
	2	[1.8; 3.3]	[6.5e−7; 3.1e−6]	[1.5e−4; 1.1e−4]	[2.0e−5; 3.3e−4]	[7.2e−4; 1.1e−3]	[1.3e−3; 2.2e−3]
	3	[1.1; 2.7]	[3.6e−7; 2.7e−6]	[2.0e−4; 8.3e−5]	[1.2e−4; 2.6e−4]	[6.5e−4; 9.3e−4]	[7.5e−4; 1.7e−3]
	4	[0.4; 2.5]	[3.6e−7; 2.7e−6]	[2.1e−4; 7.6e−5]	[1.6e−4; 2.4e−4]	[4.5e−4; 8.8e−4]	[2.1e−4; 1.6e−3]
	5	[0.2; 0.7]	[2.5e−7; 1.7e−6]	[2.0e−4; 4.0e−5]	[1.2e−4; 1.4e−4]	[3.8e−4; 2.9e−4]	[1.1e−5; 3.5e−4]
	6	[0.2; 0.6]	[2.9e−7; 1.5e−6]	[2.0e−4; 4.0e−5]	[1.2e−4; 1.4e−4]	[3.9e−4; 2.6e−4]	[2.2e−5; 3.0e−4]

Table 8: Orbit determination results as a function of network of sensors and observation batch (#) expressed in terms of error and standard deviation of semi-major axis ($[\varepsilon_a; \sigma_a]$), eccentricity ($[\varepsilon_e; \sigma_e]$), inclination ($[\varepsilon_i; \sigma_i]$), RAAN ($[\varepsilon_\Omega; \sigma_\Omega]$), AoP ($[\varepsilon_\omega; \sigma_\omega]$) and true anomaly ($[\varepsilon_\vartheta; \sigma_\vartheta]$). Values are computed at $t_{\mathrm{TDM},f}$. Errors are computed with respect to $\boldsymbol{k}_{\mathrm{FD}}$.

tion, provided that the coverage of the revolution arc is large enough. Finally, if we analyse the variability of our re-entry prediction considering all the sensors at the end of the two nights, we can see that it is extremely small, passing from 2024-09-08T18:47:36.0 UTC of batch 4 to 2024-09-08T18:47:36.6 UTC of the last batch.

Table 8 shows the OD results for all the analysed scenario as expressed in terms of error and standard deviation of semi-major axis ($[\varepsilon_a; \sigma_a]$), eccentricity ($[\varepsilon_e; \sigma_e]$), inclination ($[\varepsilon_i;\sigma_i]$), RAAN ($[\varepsilon_\Omega; \sigma_\Omega]$), AoP ($[\varepsilon_\omega; \sigma_\omega]$) and true anomaly ($[\varepsilon_\vartheta; \sigma_\vartheta]$). Values are computed at the epoch of last available observation $t_{\mathrm{TDM},f}$, namely 2024-09-08T02:03:03.4 UTC. Errors are computed with respect to FD post-event prediction $\boldsymbol{k}_{\mathrm{FD}}$, namely [71 113.5 km, 0.909, 150.33 deg, 39.96 deg, 256.64 deg, 187.88 deg]. The trends highlighted in Table 7 are evident also here, i.e. the prediction generally improves as the observed arc length and the number of participants increase. As an example, the error in semi-major axis estimate obtained by the $AIUB_1$ network passes from 9.5 km of batch 1 to 0.1 km of batch 6. Similar considerations can be made for the estimated uncertainty of the solution, which shrinks as the prediction improves. This trend is very evident for single-sensor networks. If we look again at the $AIUB_1$ case, we can see that the estimated semi-major axis standard deviation passes from 43.1 km of batch 1 to 1.2 km at the end of the two nights. Similar trends can be identified in the other Keplerian parameters. In the multiple-sensor case, the trend is the same, but the solution obtained during the early batches is way more accurate, and the uncertainty smaller. As an example, the error and estimated uncertainty in semi-major axis at the end of batch 1 when all sensors are involved are 0.3 km and 4.5 km, respectively, which further decrease to 0.2 km and 0.6 km at the end of the two nights. It is also interesting to notice how the error or difference with respect to the telemetry-based prediction is generally well included in the estimated 3σ uncertainty for all Keplerian parameters. This happens almost in all cases for the all parameters apart from some inclinations as computed for longer observation arcs, as for example in the case with all sensors, batch 6. Considering that the assumed reference has an uncertainty as well, the obtained result can be considered acceptable.

3.1. Inclusion of pre P-1 tracklets

Once analysed the accuracy of the solution obtained using only post P-1 observations, it is now interesting to investigate how the inclusion of pre P-1 tracklets would affect the accuracy and uncertainty of the re-entry prediction. For the analysis, only tracklets acquired between P-2 and P-1 (here referred to as [P-2; P-1] tracklets) were considered. Specifically, two tracklets are available: a first one measured by OES35, and a shorter one by

[P-2; P-1] sensor	$\text{Epoch}_{\text{TDM},0}$	$\text{Epoch}_{\text{TDM},f}$	ϑ_0 (deg)	ϑ_f (deg)
OES35	2024-09-04T18:56:57.5	2024-09-04T20:37:44.6	164.9	167.1
CAHA	2024-09-05T03:15:16.4	2024-09-05T03:23:50.9	173.6	173.7

Table 9: [P-2; P-1] tracklets duration in terms of initial and final epochs $\text{Epoch}_{\text{TDM},0}$ and $\text{Epoch}_{\text{TDM},f}$ and initial and final true anomalies ϑ_0 and ϑ_f. All epochs are UTC.

[P-2; P-1] sensors	$RMSE_\alpha$ (arcsec)	$RMSE_\delta$ (arcsec)	$wRMSE$	n_{acc}	n_{rej}	$\hat{c}_d$	$\hat{\sigma}_{c_d}$
OES35	0.557	0.563	0.518	1884	0	1.96	2.7e−2
CAHA	0.264	0.175	0.207	1620	0	2.15	3.7e−2
OES35, CAHA	0.593	0.671	0.586	1920	0	1.68	1.2e−2
-	0.266	0.176	0.209	1584	0	-	-

Table 10: Orbit determination results when including [P-2; P-1] tracklets (all post P-1 tracklets considered). Results are parametrised with respect to the considered [P-2; P-1] participants, and expressed in terms of root mean square error in α and δ $RMSE_\alpha$ and $RMSE_\delta$, weighted root mean square error $wRMSE$, number of accepted and rejected measurements n_{acc} and n_{rej}, and mean value and standard deviation of estimated drag coefficient $\hat{c}_d$ and $\hat{\sigma}_{c_d}$.

[P-2; P-1] sensors	$[\varepsilon_a; \sigma_a]$ (km)	$[\varepsilon_e; \sigma_e]$ (-)	$[\varepsilon_i; \sigma_i]$ (deg)	$[\varepsilon_\Omega; \sigma_\Omega]$ (deg)	$[\varepsilon_\omega; \sigma_\omega]$ (deg)	$[\varepsilon_\vartheta; \sigma_\vartheta]$ (deg)
OES35	[3.2; 5.4]	[7.4e−6; 1.4e−5]	[6.0e−5; 3.9e−5]	[2.3e−4; 2.9e−4]	[1.3e−3; 1.9e−3]	[1.5e−3; 2.6e−3]
CAHA	[0.2; 5.7]	[4.1e−7; 1.4e−5]	[2.0e−4; 3.9e−5]	[1.2e−4; 2.7e−4]	[4.2e−4; 2.1e−3]	[5.1e−5; 2.8e−3]
OES35, CAHA	[7.9; 4.6]	[1.9e−5; 1.4e−5]	[4.2e−5; 4.9e−5]	[4.6e−4; 3.6e−4]	[3.1e−3; 1.5e−3]	[3.8e−3; 2.0e−3]
-	[0.2; 0.6]	[2.9e−7; 1.5e−6]	[2.0e−4; 4.0e−5]	[1.2e−4; 1.4e−4]	[3.9e−4; 1.5e−3]	[2.2e−5; 2.0e−3]

Table 11: Orbit determination results when including [P-2; P-1] tracklets (all post P-1 tracklets are considered). Results are parametrised with respect to the considered [P-2; P-1] participants, and expressed in terms of error and standard deviation of semi-major axis ($[\varepsilon_a; \sigma_a]$), eccentricity ($[\varepsilon_e; \sigma_e]$), inclination ($[\varepsilon_i; \sigma_i]$), RAAN ($[\varepsilon_\Omega; \sigma_\Omega]$), AoP ($[\varepsilon_\omega; \sigma_\omega]$) and true anomaly ($[\varepsilon_\vartheta; \sigma_\vartheta]$). Values are computed at $t_{\text{TDM},f}$. Errors are computed with respect to $\boldsymbol{k}_{\text{FD}}$.

CAHA. Details are reported in Table 9. The analysis here presented shows how the OD results change by processing all post P-1 observations and different combinations of [P-1; P-2] tracklets.

The OD fitting follows a two-phases procedure. In the first step, the fitting process is performed by including the drag coefficient in the set of variables to estimate. The results obtained by processing all post P-1 tracklets and different combinations of [P-2; P-1] tracklets are shown in Table 10. The table reports the root mean square error in α and δ $RMSE_\alpha$ and $RMSE_\delta$, the weighted root mean square error $wRMSE$, the number of accepted and rejected measurements n_{acc} and n_{rej}, and the mean value and standard deviation of the estimated drag coefficient $\hat{c}_d$ and $\hat{\sigma}_{c_d}$. Three different cases for the [P-2; P-1] tracklets are analysed: OES35-only, CAHA-only, and both OES35 and CAHA. In addition, the results obtained by processing only post P-1 observations are reported as a term of comparison. As can be seen, the fitting obtained by adding only the short CAHA tracklet is better than the other two, and leads to root mean square errors very close to the post P-1 case. When the longer OES35 tracklet is included, instead, root mean square errors more than double are obtained. Nevertheless, all measurements are accepted in all three cases. The described behaviour can be probably explained by looking at the duration of the tracklets. The tracklet from CAHA is made of few data points covering 0.1 deg in true anomaly variation, thus from the fitting point of view can be interpreted as a single data point. The OES35 tracklet covers instead one hour and a half and 2.2 deg in true anomaly, which could be enough to have a preliminary orbit determination. The fitting process tries to correct errors in the modelling of the atmospheric perturbation by using the drag coefficient as a scaling factor for the density. This is confirmed by looking at the estimated values of c_d, which are completely different in the three cases. This scaling action, which seems enough to fit a short pre P-1 tracklet, is apparently not sufficient to compensate for possible other simplifications our atmospheric model relies on, as neglecting the actual shape and attitude of the spacecraft, when a longer pre P-1 arc is fitted. As a result, the obtained results end up being dependent on the selected pre P-1 tracklets, and are completely different in terms of residuals.

Once estimated the drag coefficient, the orbit determination process is repeated, by setting this time the drag coefficient as consider parameter [6]. The nominal value is taken from phase 1, whereas its uncertainty is set by combining $\hat{\sigma}_{c_d}$ with an assumed uncertainty for the atmospheric model. Following the assumptions done since the beginning, a 50% of the estimated c_d value is assumed as 3σ of the assumed c_d Gaussian distribution. Table 11 shows the results of the second OD phase in terms of errors and estimated standard deviations in Keplerian parameters. The trend of the errors closely resembles the one identified in Table 10. More specifically, the CAHA-only case has errors in all Keplerian parameters that are in

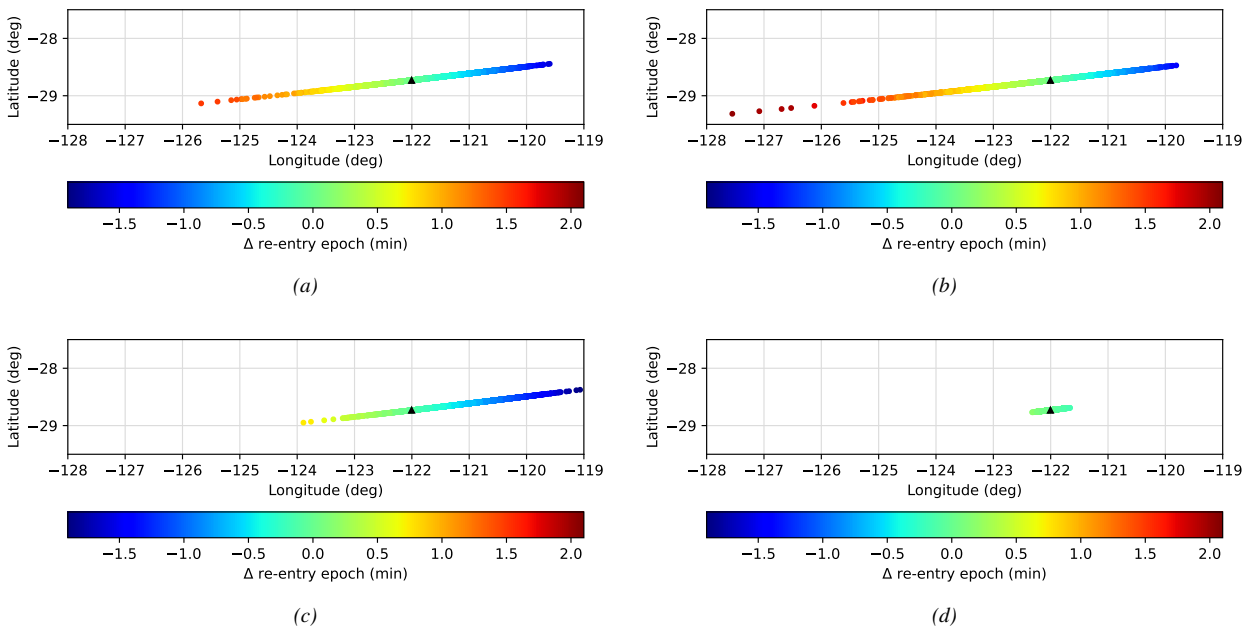

Figure 3: Re-entry latitude-longitude distribution (all post P-1 tracklets considered);(a), (b), (c) OD performed including [P-2;P-1] tracklets, namely from OES35 only (a), CAHA only (b) and both OES35 and CAHA (c), respectively; (d) OD performed on post P-1 only observations. The FD post-event prediction is reported as a black traingle. Errors in re-entry epoch are computed with respect to the FD reference, i.e. 2024-09-08T18:47:37.2 UTC

line with those obtained by processing post P-1 data only. Conversely, the results obtained by fitting a longer pre P-1 tracklet are characterised by errors in almost all Keplerian parameters that are one order of magnitude larger than those obtained with our baseline solution. Another interesting aspect is the magnitude of the estimated uncertainty, which is, for all three cases including [P-2; P-1] tracklets, one order of magnitude larger than what was obtained by processing only post P-1 data. This is obviously expected and determined by the assumed uncertainty in the consider parameter c_d. Should such uncertainty be set to lower values, the resulting Keplerian parameters uncertainty would shrink as well, eventually collapsing to the post P-1 result in case a perfect model for the drag perturbation was considered. Another aspect that is worth mentioning is the relative magnitude of the error with respect to the estimated uncertainty. As can be seen, the CAHA-OES35 case is the most critical one, having an error in semi-major axis outside the estimated 1σ interval, while for the other components the error is generally smaller or comparable with the 1σ uncertainty.

In order to understand how these uncertainties in Keplerian parameters would map into uncertainties in re-entry location and epoch, a further analysis was done. Samples were drawn from the assumed Gaussian distribution of the OD state and consider drag coefficient by relying on a standard Monte Carlo (MC) method. Once generated, each sample was propagated from OD epoch till re-entry, and the resulting propagated state vector converted into geodetic latitude and longitude and stored with its associated re-entry epoch. The analysis was repeated for all the selected configurations of [P-2; P-1] participants, along with our baseline with post P-1 only data. The results are shown in Fig. 3. The plots show the distribution in latitude and longitude at re-entry epoch as obtained by drawing 5000 MC samples. The reference re-entry location as derived from FD post-event prediction, namely β_{FD}={−122.005 deg, −28.730 deg}, is reported as a black triangle. A colormap shows the difference in estimated re-entry epoch with respect to our reference. As can be seen, by including [P-2; P-1] tracklets, the spread in re-entry spot would go up to around 8 deg in longitude and 1 deg in latitude for all the three cases, while the maximum delta in estimated re-entry epochs would reach almost 4 min. If we compare these figures with what is obtained with post P-1 data only (Fig. 3d), where the spread in longitude and latitude is 0.65 deg and 0.08 deg, respectively, and the variation in re-entry epoch is of few seconds, the effects of the assumed atmospheric uncertainty are quite evident.

Figure 4 shows the distributions of the error in re-entry latitude, longitude, and epoch when processing all post P-1 tracklets and considering as [P-2; P-1] participants both CAHA and OES35 (Figs. 4a, 4c and 4e) or none (Figs. 4b, 4d and 4f). As can be seen, the criticalities resulting from adding [P-2; P-1] tracklets are quite evident, leading to larger errors and significantly larger spreads. By looking at the plots on the left, we can notice a bias, which is particularly marked for longitude and epoch. What is also interesting to see is that the reference (the value 0.0) is still included in the distribution, but lies on the tails of it, which is not unexpected, considering the relative magnitude of the semi-major axis error and uncertainty previously described. Overall, when adding [P-2; P-1] tracklets, the mean error in latitude passes from 0.002 deg to 0.111 deg, while the standard deviation in-

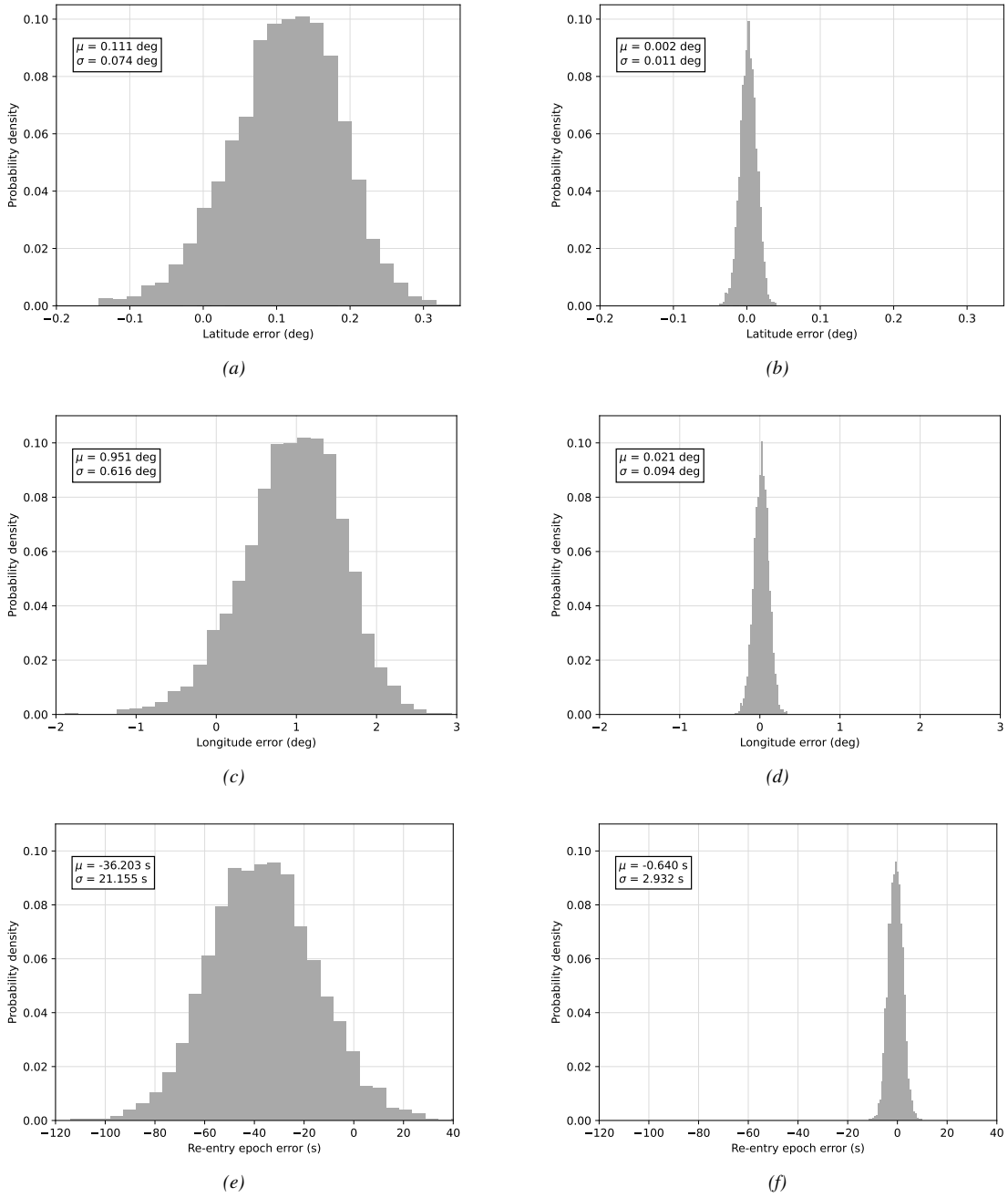

Figure 4: Estimated re-entry latitude ((a);(b)), longitude ((c);(d)) and epoch ((e);(f)) error distributions (all post P-1 tracklets considered);(a), (c), (e) OD performed including [P-2;P-1] tracklets from both OES35 and CAHA; (b), (d), (f) OD performed on post P-1 only observations. Errors in latitude, longitude and re-entry epoch are computed with respect to the FD reference, namely −28.730 deg, −122.005 deg, and 2024-09-08T18:47:37.2 UTC, respectively.

creases of a factor 7, from 0.011 deg to 0.074 deg. The degradation of the results is more marked for the longitude, with the error passing from 0.021 deg to 0.951 deg and the standard deviation inflating from 0.094 deg to 0.616 deg, and becomes apparent for the re-entry epoch, with an error increasing of a factor 50 from -0.640 s to -36.203 s and a standard deviation passing from 2.932 s to 21.155 s. Overall, by comparing the two approaches, the advantages obtained by neglecting pre P-1 tracklets are quite evident.

As a final analysis, it is interesting to see whether the inclusion of pre P-1 data could lead to better solutions if a scaling or "forgetting factor" was used to inflate the uncertainty of pre P-1 data, thus down-weigthing them. The analysis is shown in Table 12 for the CAHA and OES35 case. The table shows the error and estimated uncertainty in Keplerian parameters with increasing values

f	$wRMSE$	$[\varepsilon_a;\, \sigma_a]$ (km)	$[\varepsilon_e;\, \sigma_e]$ (-)	$[\varepsilon_i;\sigma_i]$ (deg)	$[\varepsilon_\Omega;\, \sigma_\Omega]$ (deg)	$[\varepsilon_\omega;\, \sigma_\omega]$ (deg)	$[\varepsilon_\vartheta;\, \sigma_\vartheta]$ (deg)
1	0.586	[7.9; 4.6]	[1.9e−5; 1.4e−5]	[4.2e−5; 4.9e−5]	[4.6e−4; 3.6e−4]	[3.1e−3; 1.5e−3]	[3.8e−3; 2.0e−3]
1e1	0.214	[0.8; 5.6]	[1.8e−6; 1.4e−5]	[2.0e−4; 4.7e−5]	[9.9e−5; 2.2e−4]	[6.2e−4; 2.1e−3]	[3.2e−4; 2.7e−3]
1e2	0.190	[0.2; 5.6]	[3.5e−7; 1.4e−5]	[2.0e−4; 4.8e−5]	[1.2e−4; 2.2e−4]	[4.0e−4; 2.1e−3]	[3.9e−5; 2.7e−3]
1e3	0.190	[0.2; 4.2]	[3.4e−7; 1.0e−5]	[2.0e−4; 4.4e−5]	[1.2e−4; 1.8e−4]	[4.0e−4; 1.6e−3]	[3.6e−5; 2.0e−3]
1e4	0.190	[0.2; 0.6]	[3.4e−7; 1.6e−6]	[2.0e−4; 3.9e−5]	[1.2e−4; 1.3e−4]	[4.0e−4; 2.7e−4]	[3.6e−5; 3.1e−4]
∞	0.209	[0.2; 0.6]	[2.9e−7; 1.5e−6]	[2.0e−4; 4.0e−5]	[1.2e−4; 1.4e−4]	[3.9e−4; 2.6e−4]	[2.2e−5; 3.0e−4]

Table 12: Orbit determination result sensitivity to forgetting factor f as applied to [P-2; P-1] tracklets. The considered tracklets are all post P-1 tracklets and CAHA and OES35 [P-2; P-1] tracklets. Results are expressed in terms of measurement weighted root mean square error $wRMSE$, and error and standard deviation of semi-major axis ($[\varepsilon_a;\, \sigma_a]$), eccentricity ($[\varepsilon_e;\, \sigma_e]$), inclination ($[\varepsilon_i;\sigma_i]$), RAAN ($[\varepsilon_\Omega;\, \sigma_\Omega]$), AoP ($[\varepsilon_\omega;\, \sigma_\omega]$) and true anomaly ($[\varepsilon_\vartheta;\, \sigma_\vartheta]$). Values are computed at $t_{\mathrm{TDM},f}$. Errors are computed with respect to $\boldsymbol{k}_{\mathrm{FD}}$.

of the forgetting factor f. As can be seen, as the value increases, the solution progressively converges to the post P-1 one (∞), with a decreasing trend for the estimated uncertainty. However, there seems to be no improvement in the OD solution with respect to our baseline results, and no justification in adding extra data, at least in this case. This is however an aspect that would be worth investigating more, maybe by considering longer portions of the pre P-1 arc, and studying the variability of the solution with the number of revolutions considered.

4. CONCLUSION

This paper analysed the optical sensors-based OD results obtained during the re-entry prediction campaign of CLUSTER-II-FM6. A detailed justification of the adopted orbit determination strategy was offered, and a sensitivity analysis presented, showing the impact of number of tracklets and observers on the accuracy of the results. The effect of the inclusion of tracklets observed before the last perigee pass in the OD fitting was also analysed, showing the variability of the results as a function of the selected tracklets and the resulting degradation in the accuracy of the re-entry prediction indexes. The campaign was a successful experiment that demonstrated the feasibility of optical-only re-entry predictions for this kind of orbits. Given the upcoming re-entry of the other three components of the CLUSTER quarter, and the looming possibility of losing their telemetry data in any moment, the outcome of this experience may justify the attempt to repeat the airborne experiment also with the other three spacecraft. The decision will be taken in the next months, and only then it will be clear if there are the conditions of verifying the replicability of the experiment.

ACKNOWLEDGMENTS

The authors acknowledge the contribution of ESA Flight Dynamics team and their outstanding support throughout the whole re-entry campaign.

REFERENCES

1. Sanvido, S., Losacco, M., Lemmens, S., Bastida Virgili, B., Jilete, B., Meyers, P., Hawkins, S., Letizia, F., Siminski, J., Escoubet, C.P,, Sousa, B., Sieg, D., Guerra, L., Abascal Palacios, B., Bringing SALSA Home: CLUSTER-II-2 Re-entry Strategy, Proc. 9th European Conference on Space Debris, 2025.
2. PDO activities on Salsa reentry, 2025. URL https://neo.ssa.esa.int/-/pdo-activities-on-salsa-reentry
3. Briyukhovetskyii, O., Kozhukhov, O., Ozerian, A., Kozhukhov, D., Kononchuk, I., Khlamov, S., New astronomical image processing software - first results of using, Proc. 9th European Conference on Space Debris, 2025.
4. Cordelli, E., Lauber, P., Prohaska, M., Rodriguez, J., Schlatter, P., Schildknecht, T., Recent developments at the Swiss optical ground station and geodynamics observatory Zimmerwald, Proc. 1st NEO and Debris Conference, 2019.
5. Alarcón, J.R., Klinrkrad, H., Cuesta, J., Martinez, F.M., Independent orbit determination for collision avoidance, Proc. 4th European Conference on Space Debris, 2005.
6. Tapley, B.D., Schutz, B.E., Born, G.H., "Statistical Orbit Determination", Elsevier Academic Press, 2004.